Industrial Chemistry & Materials

Accepted Manuscript

This article can be cited before page numbers have been issued, to do this please use: Y. Liu, Z. Yang, R. Zhang, Y. Lai, Y. Zhang and G. Zhang, *Ind. Chem. Mater.*, 2026, DOI: 10.1039/D5IM00302D.

View Article Online
DOI: 10.1039/D5IM00302D

ARTICLE

Highly conjugated 2D COF/MOF composites for bifunctional electrocatalytic alkaline HER and OER with enhanced activity and stability

Received 00th January 20xx,
Accepted 00th January 20xx

DOI: 10.1039/x0xx00000x

Yang Liu,[ab] Zhao-Di Yang,*[a] Rui Zhang,[a] Yingchao Lai,[a] Yu Zhang*[b] and Guiling Zhang[a]

Electrocatalytic water splitting, consisting of anodic oxygen evolution reaction (OER) and cathodic hydrogen evolution reaction (HER), represents a promising renewable energy technology for producing ultra-high purity hydrogen through efficient energy conversion and storage. However, the practical implementation of this technology in alkaline environments is hindered by the sluggish kinetics of both HER and OER, which significantly limit water splitting efficiency. The development of highly active and stable alkaline HER/OER electrocatalysts is urgently needed yet remains challenging. In this work, we synthesized a novel two-dimensional (2D) highly conjugated COF/MOF composite (COF-C_4N/THQ-M) through a post-synthesis method. This method enables controlled growth of part of COF-C_4N at the edges of THQ-M MOF to prevent structural disintegration of THQ-M, consequently to enhance surface charge transfer efficiency and further to improve catalytic activity and stability. By regulating metal sites, COF-C_4N/THQ-Co and COF-C_4N/THQ-Co_2Fe_1 are proposed to be optimal alkaline HER electrocatalysts with an overpotential of 58 mV at -10 mA cm^{-2} and alkaline OER electrocatalyst with 314 mV at 10 mA cm^{-2}, respectively, superior to most of the reported non-precious metals electrocatalysts. The charge transfer characteristics and the pathways of alkaline HER and OER were calculated based on DFT calculations to reveal the synergistic mechanism of COF-C_4N and THQ-M. This work provides a novel idea for developing high-performance bifunctional electrocatalysts for alkaline water splitting applications based on hybrid highly conjugated COF/MOF systems.

Keywords: Two-dimensional covalent organic framework; Metal-organic framework; COF/MOF composite; Electrocatalytic oxygen evolution reaction; Electrocatalytic hydrogen evolution reaction.

1. Introduction

Hydrogen energy, as an environmentally friendly fuel with high energy density and non-polluting combustion products, is regarded as an ideal energy resource to replace fossil fuels.[1-3] Electrocatalytic water splitting, consisting of an anodic OER and a cathodic HER, is a promising renewable energy conversion and storage technology to produce ultra-high purity hydrogen, which has attracted much attention.[4-7] The OER process requires a complex multi-step electron/proton reaction, and the slow kinetic rate constrains the overall performance of electrochemical energy conversion devices.[8] Electrocatalytic alkaline HER has also been extensively studied due to its favorable reaction kinetics for the water splitting - an anode half-reaction.[9-11] However, the kinetic steps of HER under alkaline conditions are relatively more complicated than acidic HER.[12] The alkaline HER process provides a source of protons through hydrolysis dissociation, and the breaking of the OH-H bond of

[a] *Heilongjiang Provincial Key Laboratory of CO_2 Resource Utilization and Energy Catalytic Materials, School of Materials Science and Chemical Engineering, Harbin University of Science and Technology, Harbin, Heilongjiang, 150080, China.*
E-mail: yangzhaodi@163.com
[b] *Institute of Process Engineering, Chinese Academy of Sciences, Beijing, 100080, China.*
E-mail: zhangyu@ipe.ac.cn
† Electronic Supplementary Information (ESI) available: [figures of XRD patterns, FTIR spectra, XPS spectra, UV-Vis spectrum, Mott-Schottky plots and bandgap, SEM, tables of ICP-OES]. See DOI: 10.1039/x0xx00000x

View Article Online
DOI: 10.1039/D5IM00300D

the water molecule may introduce additional energy barriers that greatly hinder the alkaline HER reaction rate.[13, 14] Even the HER rates of Pt catalysts in alkaline media are several orders of magnitude lower than in acidic media.[15, 16] Therefore, the splitting of water molecules needs to be promoted to accelerate the slow kinetics of alkaline HER. It was shown that the adsorption and desorption of water during electrocatalytic alkaline HER correspond exactly to the adsorption and desorption of hydroxyl groups.[16, 17] Stronger OH binding ability of catalysts facilitates the polarization of water molecules and lengthens the OH-H bond, thus greatly facilitating water splitting.[18, 19]

Currently, the OER and HER electrocatalysts are still noble metal Ir/Ru-based and Pt-based materials, but their expensive and rare features limit their scale-up applications.[20, 21] It was found that transition metal iron-, cobalt-, and nickel-based materials[22] exhibited excellent OER catalytic activities in alkaline media. The low-coordinated metal sites on the surfaces of these compounds are suitable for chemisorption and dissociation of intermediates (OH* and OOH*), which are essential for alkaline HER and OER. However, it remains challenging to explore highly active and stable OER and HER electrocatalysts in alkaline media.

MOFs have attracted more attention due to their high specific surface area, homogeneous pore size distribution, and diversified structures,[23] and have had a wide range of applications.[24, 25] In recent years, MOFs with high activity in the catalytic field have been designed and constructed by selecting different metal centers and specific organic ligands. They are widely applied in different types of electrocatalytic reactions, such as HER, hydroxide reaction (HOR), oxygen reduction reaction (ORR), and OER.[26-29] However, most of the MOFs have poor electrical conductivity, low intrinsic activity, and a limited mass transfer due to their microporous structures.[30] MX_4 (M is a transition metal; X = NH, O, S) family is commonly applied to build 2D semiconductive MOF materials. The orbital interactions can be significantly modulated by changing the metal and the coordinating atoms (X), thus effectively tuning the electronic structures of the framework.[31-33] Most of the reported MX_4 MOFs are coordinated to metals via NH or S, and extending the coordinating atoms to oxygen analogs is synthetically challenging. In 2018, Bao et al. utilized Cu(II) salt with tetrahydroxy-1,4-quinone (THQ) to generate a highly conjugated conductive 2D MOF ($Cu_3(C_6O_6)_2$), which has high conductivity.[34] In 2020, Chen et al. synthesized a redox-active 2D copper-benzoquinone (Cu-THQ) MOF using a simple solvothermal method with good electrochemical activity, high reversible capacity, and good cycling stability.[35] These studies about the structure-property relationship provide new opportunities for electronics, sensing, and energy-related applications.

Furthermore, the electrocatalytic performance of MOFs was enhanced by the strategy of forming composites with other catalytically active materials. Zeng et al. reported core-shelled Co-COF and MIL-88A-MOF-based composite catalysts for OER. The synergistic interaction between the COF-shell and MOF-core resulted in a higher catalytic activity than the single COF and MOF.[36] Xu et al. similarly designed COF and MOF heterostructures and realized core-shell structure carbon frameworks by direct pyrolysis of TP-BPY-COF@ZIP-67.[37] The COF shell layer prevented the collapse and aggregation of ZIF-67 and improved the electrical conductivity, realizing a bifunctional ORR and HER catalytic performance. These works provide ideas for the design and preparation of novel COF/MOF composite electrocatalysts. Current methods for preparing COF/MOF composites include direct condensation, post-synthesis modification, in situ, and π-π stacking.[38-40] Li et al. achieved a highly matching COF/MOF-5 composite through a "plug-socket anchoring" strategy. After grafting $-NH_2$ on the surface of MOF-5, a homogeneous and stable COF shell was constructed while maintaining the crystallinity of MOF.[41] Co-COF@MOF was obtained by growing TP-BPY-COF on the surface of MIL-88A-MOF via an in situ strategy utilizing the bipyridine unit in the COF shell to anchor the Co ions. The catalyst exhibited only OER activity (overpotential of 328 mV in 1 M KOH).[36] Most of the COF/MOF composites are prepared by introducing MOFs containing $-NH_2$ groups on the surface during the synthesis of COFs via Schiff base reaction. However, the limited number of MOFs containing $-NH_2$ groups themselves or capable of amino-functionalization hindered the composite of MOF and COF. Gao et al. constructed structurally stable core-shell MOF@COF composites using π-π stacking interactions.[42] With PCN-222-Co as the core, p-phenylenediamine (Pa) was homogeneously dispersed on its surface by ultrasonication, and then 1,3,5-tricarbonylresorcinol (Tp) was added to react with Pa to prepare the shell of COFs. For COF/MOF composites prepared by π-π stacking interactions, there are also some drawbacks, such as uneven distribution of COFs on the surface of MOFs. Although the current COF/MOF composite electrocatalysts have made initial progress in some fields, those with simultaneous bifunctional OER/HER in alkaline conditions are still relatively few and need to be further investigated and improved.

In 2019, our group successfully synthesized COF-C_4N using the solvothermal reaction of 2,3,6,7,10,11-triphenylhexamine 6 HCl (TPHA) and hexaketo cyclohexane octahydrate (HKH). The synthesized highly conjugated COF-C_4N displayed moderate OER activity (overpotential 349 mV at 10 mA cm^{-2}).[43] The better crystallinity and conductivity, as well as high stability under alkaline conditions, are the main reasons for its OER performance. In this work, we designed a novel highly conjugated 2D COF/MOF composite by synthesizing COF-C_4N using THQ-M as substrate (M = Co, Fe, and bimetallic Co_xFe_y) by a post-synthesis strategy, in which COF-C_4N/THQ-M displayed bifunctional catalytic activity of alkaline HER/OER, and has higher catalytic activity for HER/OER than single THQ-M and COF-C_4N. The HER and OER overpotentials of COF-C_4N/THQ-Co in alkaline media were 58 mV (@ -10 mA cm^{-2}) and 339 mV (@ 10 mA cm^{-2}), respectively, superior to most of the non-precious

View Article Online
DOI: 10.1039/D5IM00302D

metal catalysts. COF-C_4N/THQ-Co_2Fe_1 also shows good bifunctional HER/OER activity, with HER and OER overpotentials of 132 mV (@ -10 mA cm^{-2}) and 314 mV (@ 10 mA cm^{-2}). Density Functional Theory (DFT) calculations were carried out to reveal the synergistic mechanism in catalytic reaction pathways and charge transfer for HER and OER.

2. Results and discussion

2.1 Characterization of structures and morphologies

The composite catalyst COF-C_4N/THQ-Co was synthesized as depicted in Fig. 1a. THQ-Co was prepared with THQ and $CoCl_2{\cdot}6H_2O$ by a hydrothermal reaction at 85 ℃ for 12h.[44, 45] Then, the COF-C_4N/THQ-Co composite was obtained by putting TPHA and HKH in a COF tube containing THQ-Co by the solvothermal method. In addition, we also prepared THQ-M (M = Fe, Ni, Cu) as well as bimetallic THQ-Co_1Fe_2 and THQ-Co_2Fe_1 MOF materials and then mono/bimetallic COF-C_4N/THQ-M composites.

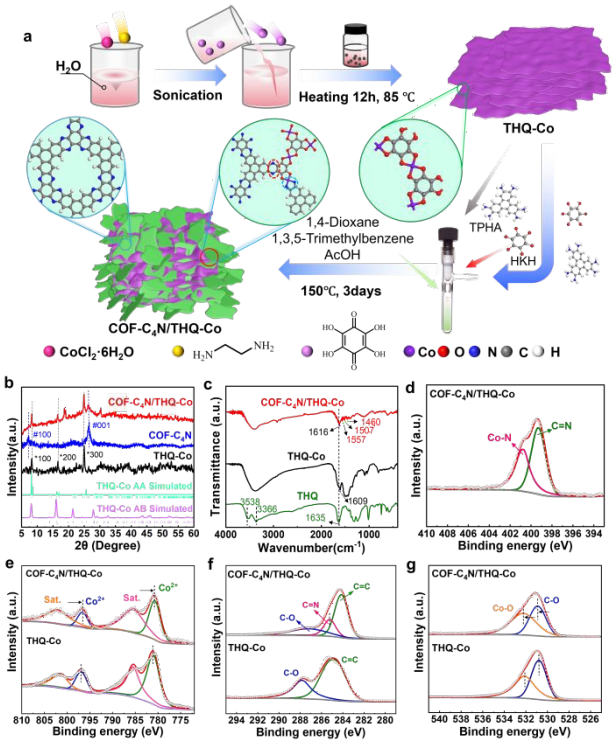

Fig. 1 (a) Schematic of the synthesis procedure of the COF-C_4N/THQ-Co composite catalysts; (b) PXRD patterns; (c) FT-IR spectra; (d) N 1s spectra of COF-C_4N/THQ-Co; (e) Co 2p, (f) C 1s, and (g) O 1s spectra of THQ-Co and COF-C_4N/THQ-Co.

The crystalline structures of the synthesized COF-C_4N, THQ-M, and COF-C_4N/THQ-M composites were characterized using powder X-ray diffraction (PXRD) measurements combined with simulation. As shown in Fig. 1b and Fig. S1†, the AA stacking pattern of THQ-Co matches well with the experimental results, and THQ-Co showed diffraction peaks at 8.23°, 16.62°, and 24.99° for (100), (200), and (300) lattice planes, respectively. By altering the metal, THQ-Fe, THQ-Cu, and THQ-Ni samples were prepared. The measured XRD pattern of THQ-Fe, THQ-Cu and THQ-Ni also showed good crystallinity, indicating the suitable preparation methods and reaction conditions (Fig. S1†). The peaks of the COF-C_4N at 2θ = 7.1° and 26.6° correspond to (100) and (001) lattice planes, respectively (Fig. 1b, blue curve).[43] The XRD pattern of the COF-C_4N/THQ-Co composite showed that the interaction between the two materials reduces the lattice order of the composite sample. This results in weakened XRD characteristic peak intensities and decreased crystallinity. However, the XRD pattern showed all the characteristic peaks of THQ-Co and the peak of 26.6° corresponding to the (001) lattice plane of COF-C_4N, indicating that the crystalline structure of THQ-Co was well preserved (Fig. 1b, red curve) and COF-C_4N keeps good interlayer structures.

The Fourier transform infrared spectroscopy (FT-IR) of the samples for TPHA, HKH, THQ, THQ-M (M = Co, Fe, Ni, Cu), bimetallic THQ-Co_1Fe_2, THQ-Co_2Fe_1, and COF-C_4N/THQ-M composites are shown in Fig. 1c and S2-S3†. Compared to THQ, the FT-IR spectra for THQ-Co displayed the elimination of OH peaks at 3538 cm^{-1} and 3366 cm^{-1}. The C=O absorption peak at 1635 cm^{-1} in THQ (Fig. 1c, green curve) has shifted toward lower wavenumbers (1609 cm^{-1}), which confirmed the efficient coordination between Co and O (Fig. 1c, black curve). The FT-IR spectra for COF-C_4N/THQ-Co manifested that all the peaks from THQ-Co were still present, the C=O absorption peak blue-shifts to 1616 cm^{-1}, while the new peaks appeared at 1560 cm^{-1}, 1508 cm^{-1}, and 1458 cm^{-1}, corresponding to the characteristic peaks of the phenazine bond (Fig. 1c, red curve). The FT-

View Article Online
DOI: 10.1039/D5IM00302D

IR spectra of the samples for other THQ-M (M = Fe, Ni, Cu), bimetallic THQ-Co_1Fe_2, THQ-Co_2Fe_1, and COF-C_4N/THQ-M composites likewise demonstrate the successful sample preparation.

The chemical and electronic states of the catalysts were analyzed by X-ray photoelectron spectroscopy (XPS). The XPS spectroscopy revealed the presence of five elements, C, N, O, Co, and Cl in COF-C_4N/THQ-Co (Fig. S4a†). The N 1s spectra of the COF-C_4N/THQ-Co sample exhibits two characteristic peaks at 400.78 and 399.28 eV, corresponding to the Co-N bond and C=N bond, respectively (Fig. 1d). Considering the preparation method of COF-C_4N/THQ-Co sample, two NH_2 groups of some TPHA may coordinate with Co, then form COF-C_4N structure at the THQ-Co edge with phenazine bond (Fig. 1a). Compared to the C=N bonding energy of COF-C_4N (400.0 eV), the bonding energy of C=N of COF-C_4N/THQ-Co (399.28 eV) exhibits a negative shift of 0.72 eV, suggesting that THQ-Co interacts with COF-C_4N (Fig. S4†). The Co 2p XPS spectra of THQ-Co and COF-C_4N/THQ-Co can be deconvoluted into four peaks (Fig. 1e). The peaks at 781.03 eV ($2p_{3/2}$) and 796.89 eV ($2p_{1/2}$) in THQ-Co, together with satellite peaks at 785.48 and 801.27 eV can be attributed to the binding energies of Co 2p of an oxidized Co^{2+} species. The Co 2p spectra of COF-C_4N/THQ-Co showed the peaks at 780.74 and 796.58 eV, and the 0.29 and 0.31 eV negative shifts relative to THQ-Co indicate the possible existence of electron transport between COF-C_4N and THQ-Co on the surface of COF-C_4N/THQ-Co, which further proves that COF-C_4N is possible to grow at the edge of THQ-Co by Co-N. The C 1s spectra of THQ-Co also reveals two characteristic peaks at 287.84 and 284.80 eV, attributed to the C-O and C=C/C-C, respectively (Fig. 1f). Compared to THQ-Co, the C 1s spectra of COF-C_4N/THQ-Co exhibits a new characteristic peak at 285.25 eV, assigned to the C=N, which is negatively shifted by 0.15 eV relative to COF-C_4N (Fig. S4b†). The shifts of C=N peaks in N 1s and C 1s spectra both verifies that COF-C_4N is possible to grow at the edge of THQ-Co through phenazine bonding during the post-synthesis process as shown in Fig. 1a. The peak at 532.08 eV in the O 1s spectrum corresponds to the O atoms bonded to metals (Co-O) from THQ-Co, indicating that the metal in THQ-Co is effectively coordinated with oxygen (Fig. 1g). In the O 1s spectrum of COF-C_4N/THQ-Co, the Co-O peak at 532.28 eV exhibits a positive shift of 0.20 eV relative to THQ-Co. This indicates that the NH_2 functional groups of COF-C_4N may coordinate with Co sites to form Co-N bonds, enhancing bond polarity and consequently increasing the binding energy. In short, the valence states of the Co in both THQ-Co and COF-C_4N/THQ-Co samples are +2. COF-C_4N grows at the edges of THQ-Co via both phenazine and Co-N bonds. Furthermore, the electron transfer capability between COF-C_4N and THQ-Co provides significant advantages for subsequent electrocatalytic reactions.

To further confirm the chemical compositions and catalytic active sites of the prepared samples, we performed Raman measurements on THQ-Co, COF-C_4N, and COF-C_4N/THQ-Co as shown in Fig. S5†. For the THQ-Co, the peaks at 1292, 1337, 1447, 1510, and 1553 cm^{-1} are assigned to the stretching vibrations of benzene rings in the organic binder and the Co-O coordination bonds formed between Co and the THQ ligands (black curve). For COF-C_4N, multiple characteristic peaks appearing near ~1500 cm^{-1} correspond to the vibration of the C=N/C-N bonds in the phenazine structure, which is a signature structural signal of COF-C_4N (blue curve). After composite formation, the Raman spectrum of COF-C_4N/THQ-Co exhibits the peaks corresponding to C-N bonds of COF-C_4N and Co-O/Co-N bonds of THQ-Co. The Co-N bonds originate from the coordination between the amino groups of TPHA and Co, indicating that COF-C_4N grows at the edges of THQ-Co via phenazine bonds and Co-N bonds (red curve).These Co-O/Co-N can also serve as active sites for subsequent HER. Additionally, the Raman curves of THQ-Co and COF-C_4N/THQ-Co exhibit a peak near approximately 450 cm^{-1}, which corresponds to the characteristic phase of $Co(OH)_2$. The $Co(OH)_2$ phase and the N sites adjacent to C in COF-C_4N synergistically act as active sites for the OER.

The Tauc plots from ultraviolet-visible diffuse reflectance spectroscopy (UV-Vis) are used to study the bandgap. The band gaps of THQ-Co, COF-C_4N, and COF-C_4N/THQ-Co are 2.83, 2.55, and 2.75 eV, respectively (Fig. S6†). Fig. S7 and S8† give the flat-band potential (E_{fb}), which was obtained from the Mott-Schottky test, and the formula obtained the conduction-band potentials: $E_{CB\ NHE,\ pH=7} = E_{fb,\ Ag/AgCl,\ pH=7} + 0.197$, the conduction band (CB) of THQ-Co, COF-C_4N, COF-C_4N/THQ-Co are -0.78, -0.35, and -0.74 eV, respectively (Fig. S9†, the Mott-Schottky results of other THQ-M and COF-C_4N/THQ-M are also given in Supporting Information). Based on the derived results from UV-Vis and Mott-Schottky, the valence band energy level (VB) of THQ-M, COF-C_4N, and COF-C_4N/THQ-M could be obtained. One can find from Fig. S9† that the introduction of Fe in COF-C_4N/THQ-Fe, COF-C_4N/THQ-Co_1Fe_2, and COF-C_4N/THQ-Co_2Fe_1 could make their CB closer to 0.0 eV(NHE), which confirms that the HER activities of COF-C_4N/THQ-Fe, COF-C_4N/THQ-Co_1Fe_2, and COF-C_4N/THQ-Co_2Fe_1 would be lower than COF-C_4N/THQ-Co. The VB level for all synthesized electrocatalysts is more positive than the OER electrical potential, so they are favorable for OER.

To confirm the sample morphology, we performed scanning electron microscopy (SEM) and transmission electron microscopy (TEM) measurements on THQ-Co, COF-C_4N, and COF-C_4N/THQ-Co. SEM images showed that the THQ-Co presented nanosheet-like structures with smaller nanosheets or agglomerated particles dispersing on the surface, and COF-C_4N also showed nanosheet-like structures with agglomeration of nanosheets (Fig. 2a and 2b, and EDS analysis of the THQ-Co displayed that the elements C, O, and Co were uniformly distributed on the surface of THQ-Co, and the content of Co was 10.68% (Fig. S10†). It was also observed that the morphology of the THQ-Co_2Fe_1 was similar to that of the THQ-Co with a nanosheet-like structure and the mass fraction ratio of Co to Fe wt.% = 10.37: 5.92, which was consistent with the mass ratio of the initial feed (Fig. S10†). The SEM image of COF-C_4N/THQ-Co samples also displayed a nanosheet-like structure with COF-C_4N dispersed on the surface and edges of THQ-Co and the lamellar agglomeration is manly due to the high plane conjugation of single-layer THQ-Co and COF-C_4N. (Fig. 2c). The EDS elemental analysis in Fig. 2d indicated that the C, N, O, and Co were uniformly dispersed in COF-C_4N/THQ-Co. Inductively Coupled Plasma-Optical Emission Spectrometry (ICP-OES) determined the Co(II) content in THQ-Co and COF-C_4N/THQ-Co to be 27.1 wt.% and 15.6 wt.%, respectively (Table S1†). The TEM images further confirmed their morphologies. One can find from TEM images in Fig. 2e and 2f that the THQ-Co presents a flimsy nanosheet, and COF-C_4N/THQ-Co is clearly composed of two flimsy layered materials, in which COF-C_4N regularly

View Article Online
DOI: 10.1039/D5IM00302D

disperses on the surface and at the edges of THQ-Co. This provides evidence from another perspective that COF-C_4N may grow at the edges of THQ-Co to lead to more active sites exposed for COF-C_4N/THQ-Co.

The porosities of THQ-Co, COF-C_4N, and COF-C_4N/THQ-Co was assessed by N_2 sorption isotherms at 77.3 K shown in Fig. S11 †. The Brunauer-Emmett-Teller (BET) surface areas of THQ-Co, COF-C_4N, and COF-C_4N/THQ-Co are 101.8, 71.8, and 50.4 $m^2 \cdot g^{-1}$, respectively. The average pore sizes of THQ-Co, COF-C_4N, and COF-C_4N/THQ-Co obtained from BJH desorption data were 14.78 nm, 8.47 nm, and 14.19 nm, respectively. Pore volumes for micropores and mesopores were determined using the HK and BJH methods, and their volume fractions were calculated as shown in Table S2 †. All samples exhibited mesopore-dominant structures. The results demonstrated that after COF-C_4N composite formation, the BET specific surface area of the COF-C_4N/THQ-Co sample decreased. COF-C_4N likely filled partial pore channels within and around THQ-Co, reducing the effective pore volume available for nitrogen adsorption. Weak interactions between the two components at the interface led to locally denser structural packing, further diminishing the BET specific surface area of the composite samples. The average pore size of the composite samples was close to that of THQ-Co, indicating that the main pore structure of THQ-Co remained largely unchanged during the composite formation process.

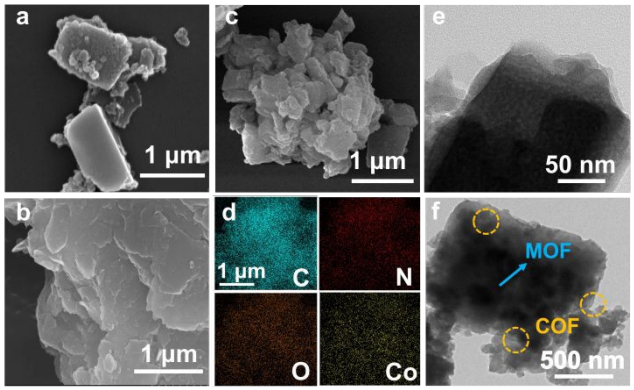

Fig. 2 SEM images of (a) THQ-Co, (b) COF-C_4N, and (c) COF-C_4N/THQ-Co; (d) EDS mappings of COF-C_4N/THQ-Co; TEM images of (e) THQ-Co and (f) COF-C_4N/THQ-Co.

2.2 Alkaline HER and OER

The electrocatalytic HER activities of THQ-M and COF-C_4N/THQ-M catalysts were investigated using a typical three-electrode system in 1 M KOH alkaline solution using carbon cloth as the catalyst carrier. The linear sweep voltammetry (LSV) curves were performed for different catalysts. In 1 M KOH, the HER overpotential of the THQ-Co is 89 mV at -10 mA cm^{-2}, and THQ-Ni and THQ-Cu did not display HER activity. THQ-Fe, THQ-Co_1Fe_2, and THQ-Co_2Fe_1 with overpotentials of 237, 203, and 189 mV at -10 mA cm^{-2}, respectively. The test results suggest that Co serves as the best alkaline HER active site for THQ-M, and bimetal sites could not increase the alkaline HER activity (Fig. 3a). In contrast, for the composite catalyst, the COF-C_4N/THQ-Co required only 58 mV to reach -10 mA cm^{-2}, and the alkaline HER activity was significantly enhanced. COF-C_4N/THQ-Fe, COF-C_4N/THQ-Co_1Fe_2, and COF-C_4N/THQ-Co_2Fe_1 with overpotentials of 188, 176, and 132 mV at -10 mA cm^{-2}, respectively, HER activity is all improved compared to the single THQ-M MOF materials. Notably, even at a high current density of -100 mA cm^{-2}, COF-C_4N/THQ-Co still has a lower overpotential than the other catalysts, further validating its excellent alkaline HER activity (Fig. 3b). To further explore the HER reaction kinetics, the Tafel slopes of the catalysts were plotted by LSV curves fitting to the linear regions of the Tafel plot ($\eta = b \log|j| + a$, where b is the Tafel slope, j is the current density, and iR is compensated at 100%) (Fig. 3c and Fig. S12a†). The Tafel slope of COF-C_4N/THQ-Co was 94.29 mV dec^{-1}, much smaller than that of THQ-Co (124.07 mV dec^{-1}), suggesting that the composite catalyst has faster HER kinetics. Moreover, the Tafel slopes of 162.3, 152.45, and 131.77 mV dec^{-1} for COF-C_4N/THQ-Fe, COF-C_4N/THQ-Co_1Fe_2, and COF-C_4N/THQ-Co_2Fe_1 were lower than those of the corresponding THQ-M samples, which demonstrates formation of COF-C_4N/THQ-M is helpful to improve the kinetics of alkaline HER.

In general, the mechanism of HER in alkaline electrolytes is divided into two parts.[47] The first part is the Volmer reaction ($H_2O + e^- \rightarrow H^*_{ads} + OH^-$), where H_2O dissociates into H adsorbed on the catalyst surface. Subsequently, the second part has two pathways: (1) the Heyrovsky step ($H^*_{ads} + H_2O + e^- \rightarrow OH^- + H_2$), where H* combines with electrons and H_2O to form hydrogen molecules; (2) the Tafel step ($H^*_{ads} + H^*_{ads} \rightarrow H_2$), where two H* atoms combine directly to form a hydrogen molecule. The Tafel slopes for the Volmer, Heyrovsky, and Tafel steps are usually considered to be 120, 40, and 30 mV dec^{-1}, respectively.[48] A smaller Tafel slope implies a faster kinetic process, suggesting that only a lower overpotential is required for the catalyst to reach the desired current. Thus, our synthesized COF-C_4N/THQ-Co composite catalysts follow the effective HER Volmer-Heyrovsky mechanism. The Heyrovsky reaction is a rate-determining step, and a larger electrode reaction area has a faster electrolysis rate.[48] In addition, the exchange current density (j_0), which is proportional to the intrinsic HER activity of the electrocatalyst, can be derived from the Tafel plot by an extrapolation method.[49,50] In particular, after being normalized by the relative surface area, the j_0 obtained for COF-C_4N/THQ-Co was 1.77×10^{-3} mA cm^{-2}, which was much larger than that of COF-C_4N/THQ-Fe (0.62×10^{-3} mA cm^{-2}), COF-C_4N/THQ-Co_1Fe_2 (0.65×10^{-3} mA cm^{-2}), and COF-C_4N/THQ-Co_2Fe_1

View Article Online
DOI: 10.1039/D5IM00302D

(0.74×10^{-3} mA cm^{-2}) exchange current densities (Fig. 3d). Thus, the j_0 data also indicate that COF-C_4N/THQ-Co shows the highest HER activity.

To better explore the origin of enhanced HER activity, the electrode area involved in the electrochemical process was revealed by electrochemical surface area (ECSA). The ECSA was determined by measuring the double-layer capacitance (C_{dl}). The C_{dl} was obtained and calculated by cyclic voltammetry (CV) at different scan rates under 1 M KOH conditions (Fig. 3e, S12b, S13, and S14†). The calculated C_{dl} value of the COF-C_4N/THQ-Co was estimated to be 96.3 mF cm^{-2}, larger than that of THQ-Co (82.6 mF cm^{-2}), COF-C_4N/THQ-Fe (65.8 mF cm^{-2}), COF-C_4N/THQ-Co_1Fe_2 (78.7 mF cm^{-2}) and COF-C_4N/THQ-Co_2Fe_1 (80.1 mF cm^{-2}) composite catalysts, indicating that COF-C_4N/THQ-Co is able to expose more catalytical active sites, and a larger ECSA corresponds to the enhanced HER catalytic activity (Fig. 3e). ECSA normalized LSV polarization curves (Fig. 3f) show the COF-C_4N/THQ-Co has higher current densities. Its overpotential is also lower than that of THQ-Co and other mono/bimetallic composite catalysts. This also indicates that the HER activity was enhanced by constructing the composite catalyst, and the Co site mainly served as the active site for alkaline HER reaction.

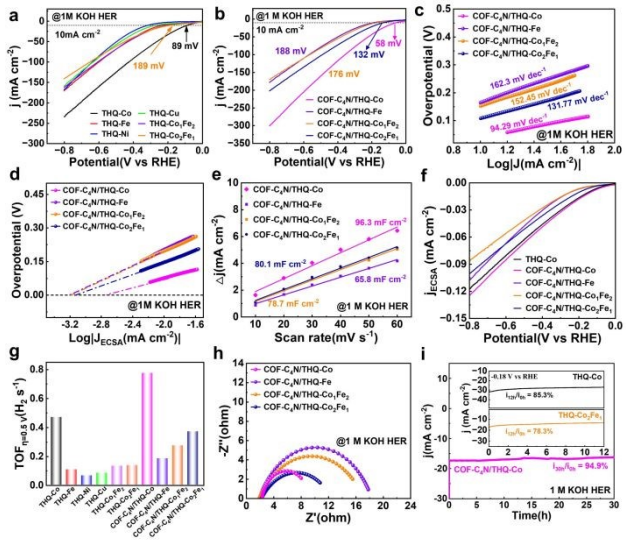

Fig. 3 (a) LSV curves of alkaline HER for different metal THQ-M; (b) LSV curves of COF-C_4N/THQ-M; (c) Tafel slopes of COF-C_4N/THQ-M; (d) The exchange current density is derived from the Tafel plot by an extrapolation method; (e) C_{dl} values of COF-C_4N/THQ-M; (f) The ECSA-normalized polarization curves of COF-C_4N/THQ-M; (g) Comparison of TOF values HER at η = 0.5 V; (h) EIS spectra of COF-C_4N/THQ-M; (i) Chronopotentiometric curves of COF-C_4N/THQ-Co at -0.11 V vs RHE for 30 h (The insets are the chronopotentiometric curves of THQ-Co and THQ-Co_2Fe_1 at -0.18 V vs RHE for 12 h)

To further elucidate the inherent HER activity of the catalyst, the turnover frequency (TOF) data were calculated. The number of active sites was determined by first performing CV in the phosphate buffer (pH = 7) at a scan rate of 50 mV s^{-1}, as reported by Chen et al.[26] The TOF of HER was calculated by the following equation: TOF(s^{-1}) = (j × A)/(2 × n × F), where j, n, F, and A are the current density of the electrocatalyst, the number of active sites on the synthesized electrodes, the Faraday constant, and the cathode surface area, respectively. Fig. 3g shows the TOF data for THQ-M and COF-C_4N/THQ-M. The COF-C_4N/THQ-Co requires lower overpotentials than the other catalysts. A TOF of 0.776 s^{-1} was obtained for the COF-C_4N/THQ-Co composite catalyst at overpotential η = 0.5 V, which is significantly higher than that of THQ-Co (0.47 s^{-1}) and other composite catalysts (Fig. S15†). Hence, the intrinsic HER activities of the composite catalysts are in order of COF-C_4N/THQ-Co > THQ-Co > COF-C_4N/THQ-Co_2Fe_1 > COF-C_4N/THQ-Co_1Fe_2 > COF-C_4N/THQ-Fe > THQ-M (except for Co), confirming that the Co metal sites have higher HER activities, and that the synergistic effect between COF-C_4N and THQ-Co resulted in an increased HER activity of COF-C_4N/THQ-Co. Moreover, electrochemical impedance spectroscopy (EIS) analysis was used to study the HER kinetics of the catalysts. The Nyquist plots (Fig. 3h and Fig. S11c†) indicated that the charge transfer resistances (R_{ct}) of all the composite catalysts are lower than that of THQ-M. The Rct of COF-C_4N/THQ-Co is 7.12 Ω cm^{-2}, which is lower than that of THQ-Co (8.90 Ω cm^{-2}), COF-C_4N/THQ-Fe (16.4 Ω cm^{-2}), COF-C_4N/THQ-Co_1Fe_2 (15.3 Ω cm^{-2}), and COF-C_4N/THQ-Co_2Fe_1 (10.2 Ω cm^{-2}). This suggests that the charge transfer kinetics of COF-C_4N/THQ-Co is faster than single THQ-Co during the HER process.

In addition to catalytic activity, stability is crucial for the practical application of catalysts. The long-term stability of the catalysts was further evaluated by continuous CV scanning for 500 cycles, and chronoamperometric tests were carried out under a constant overpotential in 1 M KOH. Fig. S16† gives the LSV polarization curves of COF-C_4N/THQ-Co composite before and after 500 CV cycles. The LSV polarization curves show little change, and the current density decay of COF-C_4N/THQ-Co is negligible after the 500 CV cycles, indicating its robust stability for alkaline HER. Furthermore, the COF-C_4N/THQ-Co display obviously enhanced stability in the chronoamperometry test in comparison with THQ-Co (85.3% for 12 h), THQ-Co_2Fe_1 (78.3% for 12 h), and COF-C_4N/THQ-Co (95.7% for 12h, Fig. S17†), maintaining a current density of 94.9%

Journal Name ARTICLE

View Article Online
DOI: 10.1039/D5IM00302D

under a constant potential test for 30 h. Therefore the composite of COF-C_4N and THQ-Co not only helps to enhanced the HER activity but also improved catalytic stability in alkaline solutions (Fig. 3i).

The electrocatalytic OER performance of the samples is also tested in alkaline media. The LSV curves of OER for THQ-M in 1 M KOH are given in Fig. 4a. It is observed that the overpotential of THQ-Co is 357 mV at 10 mA cm^{-2}, and the overpotentials of THQ-Fe and THQ-Cu are bigger (405 mV and 465 mV at 10 mA cm^{-2}). The THQ-Ni displays an oxidation peak, although negative sweeping makes its overpotential reach 308 mV at 10 mA cm^{-2}. The stability test of THQ-Co shows that the current density of the sample decreased significantly under a continuous constant potential test for 12 h, only 49.5% of the current density was maintained, and the catalytic activity decreased dramatically, which indicates the poor electrocatalytic OER stability (Fig. 4b). The XRD spectra of THQ-Co before and after electrocatalysis varied considerably, as shown in Fig. S18†, and the diffraction peaks of THQ-Co disappeared after electrocatalysis. This result indicates that the structural instability leads to poor electrocatalytic OER stability. The structure undergoes obvious changes, probably due to the Co^{2+} dislodging from the structure during prolonged testing, which leads to continuous disintegration of the structure and a gradual degradation of OER performance. In comparison, the bimetallic THQ-Co_2Fe_1 enhances the OER activity and stability moderately (322 mV at 10 mA cm^{-2}, 78.5%)(Fig. 4b). The smaller R_{ct} of the bimetallic catalysts also indicates the enhanced charge transfer kinetics, the accelerated electron transfer process, and the enhanced catalytic OER performance (Fig. S19†).

COF-C_4N/THQ-M composites were constructed and synthesized to further enhance the OER activity and stability. As observed in LSV curves in Fig. 4c, the OER overpotentials of COF-C_4N/THQ-Co, COF-C_4N/THQ-Fe, COF-C_4N/THQ-Co_1Fe_2, and COF-C_4N/THQ-Co_2Fe_1 at 10 mA cm^{-2} are 339, 322, 325, and 314 mV, respectively. The OER overpotentials of all COF-C_4N/THQ-M composites are lower than the corresponding single THQ-M. The Tafel slopes of the composites are all smaller than those of the THQ-M samples (Fig. 4d and Fig. S19a†). The Tafel slope of COF-C_4N/THQ-Co_2Fe_1 is 53.54 mV dec^{-1}, which indicates COF-C_4N/THQ-Co_2Fe_1 has a relatively faster charge transfer rate in the OER process (Fig. 4d). The calculated C_{dl} of COF-C_4N/THQ-M are found to be all higher than the corresponding single THQ-M, indicating that the COF-C_4N/THQ-M have bigger electrochemically active areas and can expose more active sites compared to THQ-M (Fig. 4e and Fig. S19-S21†). Among them, COF-C_4N/THQ-Co_2Fe_1 has the largest C_{dl} value and displays optimal OER activity. The TOF of COF-C_4N/THQ-Co_2Fe_1 is also higher than any other composite catalysts and THQ-M as given in Fig. 4f. For example, at an overpotential of 300 mV, COF-C_4N/THQ-Co_2Fe_1 achieves a TOF of 0.19 s^{-1}, which is a little higher than COF-C_4N/THQ-Co (0.078 s^{-1}), COF-C_4N/THQ-Fe (0.145 s^{-1}), COF-C_4N/THQ-Co_1Fe_2 (0.117 s^{-1}), THQ-Co (0.066 s^{-1}), and THQ-Fe (0.024 s^{-1}) (Fig. 4f and Fig. S22†). The enhanced activity of COF-C_4N/THQ-Co_2Fe_1 may be attributed to the synergistic interaction between Co and Fe. In addition, Rcts of COF-C_4N/THQ-Co, COF-C_4N/THQ-Fe, COF-C_4N/THQ-Co_1Fe_2, and COF-C_4N/THQ-Co_2Fe_1 are all smaller than the corresponding THQ-M according to Nyquist curves (Fig. 4g and Fig. S19c†). Among all composite catalysts, COF-C_4N/THQ-Co_2Fe_1 displays the smallest R_{ct} and the best conductivity for its better charge transfer. Moreover, ECSA normalized LSV polarization curves in Fig. 4h indicate that COF-C_4N/THQ-Co_2Fe_1 has the highest current density. Fig. 4i obtained from the Tafel plot by an extrapolation method show that COF-C_4N/THQ-Co_2Fe_1 displays the highest exchange current density. All these data demonstrate optimal OER activity of COF-C_4N/THQ-Co_2Fe_1.

LSV tests before and after 500 CV cycles were performed for COF-C_4N/THQ-Co, COF-C_4N/THQ-Fe, COF-C_4N/THQ-Co_1Fe_2, and COF-C_4N/THQ-Co_2Fe_1 (Fig. S23†). It is observed that the current density decay of COF-C_4N/THQ-Co is negligible after 500 CV cycles. A chronoamperometric test was subsequently performed at a constant potential to evaluate the OER stability of COF-C_4N/THQ-Co in 1 M KOH. The results show that 81.7% of the current density was maintained after 30 h (Fig. 4b). It is confirmed that forming composite catalysts is beneficial for further enhancing the alkaline OER stability.

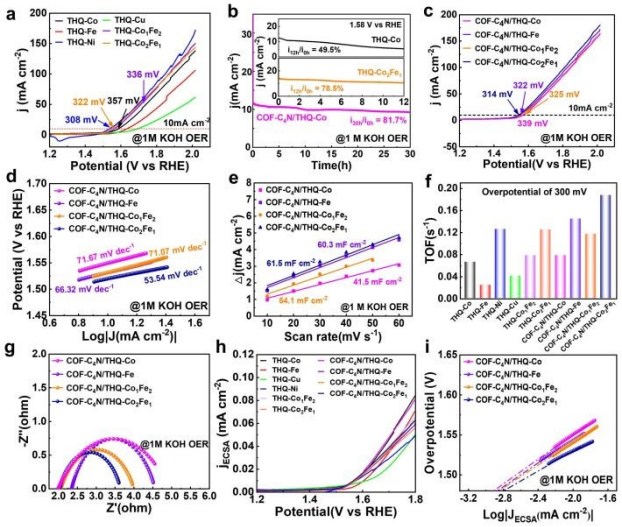

Fig. 4 (a) LSV curves of alkaline OER for different metal THQ-M; (b) Chronopotentiometric curves of THQ-Co and THQ-Co_2Fe_1 at 1.58 V vs. RHE for 12 h (The inset), Chronopotentiometric curves of COF-C_4N/THQ-Co for 30 h; (c) LSV curves of COF-C_4N/THQ-M; (d) Tafel slopes of COF-C_4N/THQ-M; (e) C_{dl} values of COF-C_4N/THQ-M for OER in alkaline media; (f) Comparison of TOF values for OER at η = 300 mV; (g) EIS spectra of COF-C_4N/THQ-M; (h) The ECSA-normalized polarization curves; (i) The exchange current density derived from the Tafel plot by an extrapolation method.

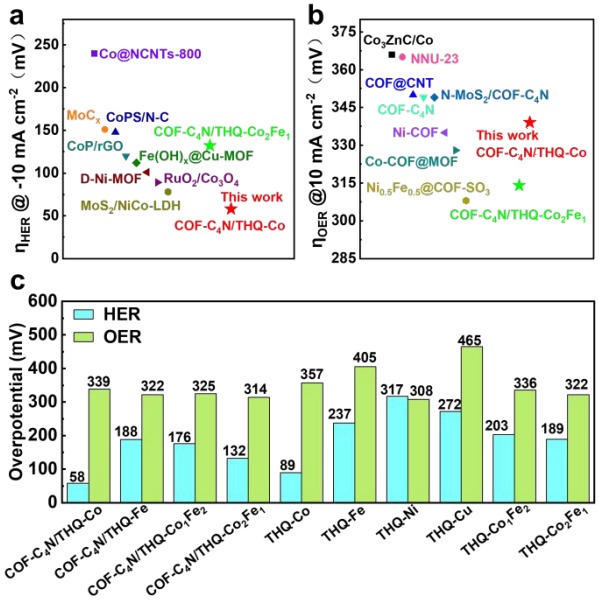

Fig. 5 Comparison of (a) OER and (b) HER activities of our catalysts with those of recently reported electrocatalysts on various substrates in an alkaline medium; (c) The HER and OER activities of different catalysts we prepared in alkaline media were compared.

To further investigate the catalytic stability of the COF-C_4N/THQ-Co sample, we performed ICP testing on the Co(II) content in COF-C_4N/THQ-Co after 500 cycles CV. The Co elemental content after HER and OER cycles was 13.54 wt% and 11.69 wt%, respectively (Table S3†). The results revealed a slight leaching of Co during the electrocatalytic cycle, which is presumed to originate from the dissociation and dissolution of active sites during the reaction process. The strong oxidative environment of the OER exacerbates Co leaching, consistent with the results from the 30 h chronopotentiometric curve of COF-C_4N/THQ-Co (Fig. 4b). This indicates that Co leaching may be one of reasons leading to a slight decrease in the OER stability. Combined with the LSV curves of COF-C_4N/THQ-Co after OER and HER 500 cycles (Fig. S16 and S23†) and the chronopotentiometric curves at 30 h, the catalytic activity did not decrease much after cycling on the whole. Therefore, although a small amount of Co leaching occurs in the COF-C_4N/THQ-Co sample, its activity and stability were not affected significantly. The COF-C_4N/THQ-Co after a 30h chronoamperometric test for HER and OER were characterized by XRD, IR, SEM, and TEM (Fig. S24-S26†). The results demonstrate that the morphology and crystal structure of COF-C_4N/THQ-Co after the stability test have slight variations in an alkaline medium compared with the pristine COF-C_4N/THQ-Co. Subsequently, XPS analysis was performed on COF-C_4N/THQ-Co samples before and after HER/OER catalysis to determine their composition. The Co 2p spectrum after HER revealed a slight shift of the Co $2p_{3/2}$ peak toward lower binding energies without broadening, indicating good structural stability of the catalyst during HER and no significant dissolution or loss of Co (Fig. S27a†). As shown in Fig. S27b†, following the OER stability test, two primary peaks at 780.03 and 782.19 eV appear in the Co $2p_{3/2}$ spectrum. The 782.19 eV peak corresponds to the Co^{3+} $2p_{3/2}$, while the satellite peak at 788.27 eV exhibits reduced intensity and a shift, confirming the presence of a small amount of residual Co^{2+}. This indicates that Co undergoes oxidation during the OER process, with low-valent Co^{2+} being oxidized to higher oxidation states. Additionally, the reduced intensity of the Co 2p peak after the reaction suggests that some Co dissolved and was lost under the high-potential and strongly alkaline OER conditions, leading to a decrease in Co content on the catalyst surface. This finding is consistent with the ICP test results.

Based on the discussions above, all four highly conjugated composites COF-C_4N/THQ-Co, COF-C_4N/THQ-Fe, COF-C_4N/THQ-Co_1Fe_2, and COF-C_4N/THQ-Co_2Fe_1 display efficient electrocatalytic bifunctional HER and OER under alkaline conditions. Comparison of alkaline HER and OER activity with other works, as shown in Fig. 5a and 5b, the alkaline HER activity of COF-C_4N/THQ-Co reaches the current optimal level (Table S4†), and the OER activities of COF-C_4N/THQ-Co and COF-C_4N/THQ-Co_2Fe_1 are comparable to those of other non-noble metal OER catalysts (Table S5†). Fig. 5c displays the comparison of OER and HER overpotentials at 10 mA cm^{-2} and -10 mA cm^{-2} for different catalysts in this work, where COF-C_4N/THQ-Co and COF-C_4N/THQ-Co_2Fe_1 are proposed to be optimal alkaline HER and OER electrocatalysts, respectively, in this work.

To further reveal the influence of synthesis method and composition mode on their electrocatalytic HER/OER activity and stability, we prepared COF-C_4N+THQ-M catalysts by simply mixing COF-C_4N samples and THQ-M samples at a mass ratio of 1:1 and then ultrasonically dispersion. The OER and HER activity of COF-C_4N+THQ-M in 1 M KOH was also tested. Fig. S28

and S29† show that the HER overpotentials of four COF-C_4N+THQ-M samples are 83, 246, 187, and 173 mV at 10 mA cm^{-2} and Tafel slopes are 120, 283, 178, and 159 mV dec^{-1}, respectively. The HER activities are all decreased relative to COF-C_4N/THQ-M. HER stability test for COF-C_4N+THQ-Co was performed as shown in Fig. S28d†, where the current density is only maintained at 71.1% under 12 h constant potential test. OER activity tests in Fig. S30 and S31 † point out the OER overpotentials of COF-C_4N+THQ-Co, COF-C_4N+THQ-Fe, COF-C_4N+THQ-Co_1Fe_2, and COF-C_4N+THQ-Co_2Fe_1 at 10 mA cm^{-2} are 346, 422, 337, and 321 mV, respectively. The current density for COF-C_4N+THQ-Co_2Fe_1 kept 79.1% under 12 h constant potential test, as shown in Fig. S30d†. Overall, the activity and stability of COF-C_4N+THQ-M are not as good as those of COF-C_4N/THQ-M, regardless of HER or OER. Fig. S32† compares the HER/OER LSV polarization curves of COF-C_4N/THQ-Co_2Fe_1 and COF-C_4N+THQ-Co_2Fe_1 prepared by two different methods. The HER activity of COF-C_4N+THQ-Co_2Fe_1 could not reach that of COF-C_4N/THQ-Co_2Fe_1 prepared by the post-synthesis method. The difference in OER activity between COF-C_4N/THQ-Co_2Fe_1 and COF-C_4N+THQ-Co_2Fe_1 is relatively small. The comparison of the activity results combined with the characterization analysis of COF-C_4N/THQ-M indicates that the post-synthesis method perhaps allows a portion of COF-C_4N to grow at the edges of THQ-M by Co-N or phenazine bonding, thereby preventing the disintegration of THQ-M structures, exposing more metal sites of THQ-M for HER/OER reaction, and effectively promoting charge transfer and separation to realize enhanced activity and stability for HER/OER.

2.3 Mechanism

The HER process in alkaline media requires the dissociation of H_2O at the catalyst surface to obtain protons. Thus, the HER process in alkaline media involves two steps (Fig. 6a), the Volmer step ($H_2O+e^- \rightarrow *H+OH^-$) and the Heyrovsky step ($H_2O+*H+e^- \rightarrow H_2+OH^-$). For alkaline HER, the first step requires proper adsorption of H_2O molecules on the catalyst surface. The H_2O adsorption step of COF-C_4N requires overcoming energy barrier of 0.108 eV, but H_2O adsorption on Co site of THQ-Co is very easy and energy-decreased process (ΔG_{H2O} = -0.563 eV as shown in Fig. 6b). Although H_2O dissociation to generate *H requires overcoming about 0.2 eV barrier for THQ-Co, H_2 desorption from Co site of THQ-Co is easier than N site of COF-C_4N by comparing $|\Delta G_{*H}|$ at the Co site and N site in Fig. S33†. The alkaline HER overpotential of COF-C_4N measured experimentally is 253 mV at 10 mA cm^{-2} (Fig. S34†), further verifying that COF-C_4N is poorly active against HER. Therefore, the above results demonstrate that Co sites are the main HER active center for both THQ-Co and composite catalyst COF-C_4N/THQ-Co. The further enhancement of HER activity for COF-C_4N/THQ-Co composite catalysts should be attributed to the increased charge transfer between COF-C_4N and THQ-Co.

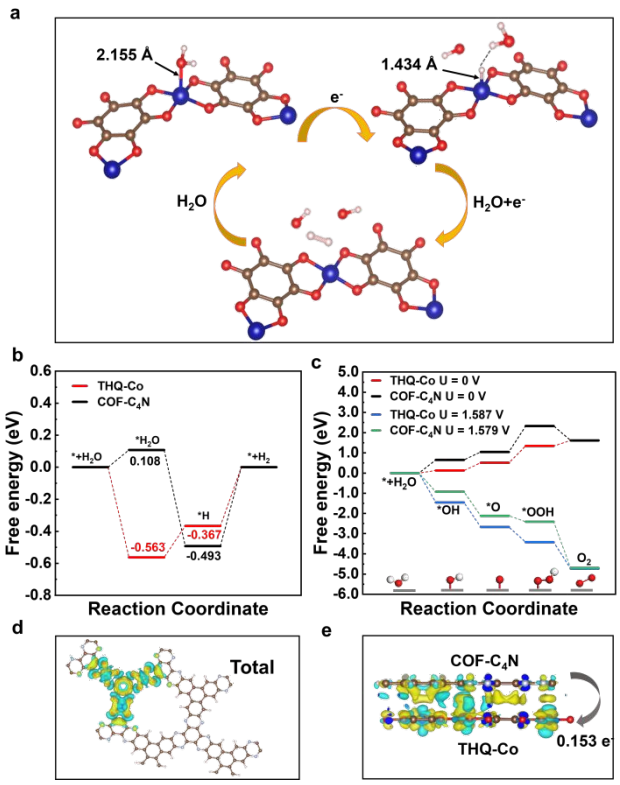

Fig. 6 Mechanisms of THQ-Co and COF-C_4N for OER and HER in alkaline media. (a) Schematic for the proposed HER pathway on the surface of the THQ-Co catalyst in alkaline media; (b) The free energy profiles for the HER process for THQ-Co and COF-C_4N catalysts in alkaline media; (c) The free energy profiles for the OER process of Co sites for THQ-Co and C4 sites for COF-C_4N at applied potential bias and U = 0 V (pH = 14); (d) Charge density difference (Δρ) for a model structure of COF-C_4N growing at the edge of THQ-Co (isovalue, 0.0025 e $Å^{-3}$), $\Delta\rho = \rho_{AB} - \rho_A - \rho_B$, set AB is the total model structure, set A is the metal atoms, and set B is the residual part after subtracting the metal atoms; (e) Charge density difference for a model structure of COF-C_4N interacting with THQ-Co with π-π

View Article Online
DOI: 10.1039/D5IM00302D

interaction, Δρ = ρ(Total)-ρ(THQ-Co)-ρ(COF-C_4N). The yellow and blue isosurfaces indicate charge accumulation and charge depletion in space, respectively.

To gain insight into OER activity, we calculated the free energy profiles of the OER pathways for THQ-Co and COF-C_4N at U = 0 V and experimentally applied bias, respectively, as shown in Fig. 6c, in which OER active sites are Co sites for THQ-Co and C4 sites for COF-C_4N[43] (The intermediate configurations in the OER pathway for THQ-Co are shown in Fig. S35†). The energy barriers of the rate-determining step *O → *OOH for both THQ-Co and COF-C_4N are 0.83 eV and 1.28 eV. When the applied bias of THQ-Co and COF-C_4N is considered, THQ-Co and COF-C_4N both show a spontaneous downslope tendency at actual applied bias 1.587 V and 1.579 V, which proves each of them displays similar OER activity at a small applied bias. The electrocatalytic OER stability of separate THQ-Co is very poor, therefore the composite of THQ-Co and COF-C_4N could not only improve the stability but also further improve the OER reaction activity because COF-C_4N could increase the number of OER active sites and accelerate the charge transfer.

In Fig. 6d and 6e, we calculated the charge density differences of COF-C_4N/THQ-Co. It is clear that electrons are more accumulated on Co sites for the model structure of COF-C_4N growing at the edge of THQ-Co, as shown in Fig. 6d. In Fig. 6e, the electrons were locally accumulated at the interface region of COF-C_4N and THQ-Co for the model structure of COF-C_4N on the surface of THQ-Co by π-π interaction, which significantly regulated the electronic structure of the COF-C_4N/THQ-Co composites, and the electrons transferred from the COF-C_4N layer to the surface of THQ-Co with 0.153 e^-. The charge density differences verified that the charge transfer abilities are enhanced and the electrons will migrate to the surface of THQ-Co to produce H_2 on Co sites.

3. Conclusions

In conclusion, two highly conjugated 2D COF-C_4N and THQ-M were firstly chosen to prepare COF/MOF composite electrocatalysts COF-C_4N/THQ-M by a post-synthesis strategy. The characterizations and tests showed that part of COF-C_4N may grow at the edge of THQ-M besides of uniformly dispersion on the surface of THQ-M. The HER and OER activity and stability in alkaline media were systematically studied and compared. The results indicate that the composite of THQ-M and COF-C_4N could not only improve the stability, but also further enhance the HER/OER reaction activity of the corresponding single THQ-M and COF-C_4N. By regulation of metal sites, COF-C_4N/THQ-Co and COF-C_4N/THQ-Co_2Fe_1 are proposed to be optimal alkaline HER and OER electrocatalysts respectively in this work. DFT calculations revealed that both THQ-Co and COF-C_4N can act as OER catalysts, and COF-C_4N in the composite catalysts COF-C_4N/THQ-Co mainly solved the instability of THQ-Co in alkaline media. The THQ-Co can act as an HER catalyst alone, but the composite with COF-C_4N realizes more effective HER activity and stability in alkaline media. Charge density difference is also calculated to verify the charge transfer in COF-C_4N/THQ-M. This study provides a new proposal for the design of highly efficient bifunctional COF/MOF composite electrocatalysts.

4. Experimental section

4.1 Chemicals and materials

All reagents were directly obtained from commercial sources without further purification. Cobalt chloride hexahydrate ($CoCl_2·6H_2O$), ferrous sulfate heptahydrate ($FeSO_4·7H_2O$), nickel acetate tetrahydrate ($Ni(OAc)_2·4H_2O$), copper(II) acetate monohydrate ($Cu(OAc)_2·H_2O$), nafion solution (5.0 wt%), sodium hydroxide, potassium hydroxide, and acetic acid were purchased from Shanghai Rinn Technology Development Co., Ltd. Iron(III) chloride hexahydrate were purchased from Tianjing HengXing Chemical Reagent Co., Ltd. Tetrahydroxyquinone was purchased from Shandong Xiya Reagent Co., Ltd. 2,3,6,7,10,11-triphenylhexamine 6 HCl and hexaketo cyclohexane octahydrate were purchased from Jilin Chinese Academy of Sciences-Yanshen Technology Co., Ltd. 3 mL of 1,3,5-trimethylbenzene was purchased from Nanning Chemical Group Co., Ltd. 1,4-dioxane was purchased from Shanghai Aladdin Biochemical Technology Co., Ltd. Carbon cloth was purchased from Suzhou Sinero Technology Co., Ltd. Graphite rod and Ag/AgCl (3.5 M KCl) electrode were purchased from AIDA Science-Technology Development Co., Ltd. All aqueous solutions were prepared using ultrapure water.

4.2 Synthesis of catalysts

Synthesis of THQ-M: THQ-M samples were synthesized according to the reported procedure with minor modifications.[44,45] In a typical synthesis of THQ-Co, 0.135 mmol of $CoCl_2·6H_2O$ was completely dissolved in 16 mL of deionized water, and then 40 μL of ethylenediamine was injected into the above solution using a pipette gun. Then, 0.29 mmol of tetrahydroxy-1,4-quinone (THQ) was completely dissolved in 16 mL of deionized water and then transferred to the above water/ethylenediamine solution under ultrasonic vibration. The mixed solution was poured into a sealed glass vial and heated at 85 ℃ for 12 h. After cooling naturally to room temperature, collect the precipitate. Wash it with water and ethanol for 30 minutes in an ultrasonic ice bath, then let it settle. Filter and wash it three times with water and acetone, respectively. Finally, vacuum dry it at 60 ℃ for 24 h to obtain THQ-Co. THQ-Fe, THQ-Ni, THQ-Cu, THQ-Co_1Fe_2, and THQ-Co_2Fe_1 were synthesized in a similar way using different $Ni(OAc)_2·4H_2O$, $Cu(OAc)_2·H_2O$, and $FeSO_4·7H_2O$, with the total amount of metal ions fixed at 0.27 mmol.

Synthesis of COF-C_4N/THQ-Co: 2,3,6,7,10,11-triphenylhexamine 6 HCl (TPHA) and hexaketo cyclohexane octahydrate (HKH) were

Journal Name ARTICLE

View Article Online
DOI: 10.1039/D5IM00303D

weighed in a mass ratio of 25.5 mg:25.0 mg. The above samples were dissolved in a mixture of 1.5 mL of 1,4-dioxane and 1.5 mL of 1,3,5-trimethylbenzene in a 10 mL tube, and 50 mg of the THQ-Co sample was added. Disperse by sonication at 25 ℃ for 30 min, then add 4 M acetic acid (0.5 mL) into the test tube and shake well. Next, three freeze-pump-thaw cycles were performed. After degassing and confinement, the reaction was carried out in a blower oven at 150 ℃ for 3 days and cooled naturally to room temperature. The precipitate is washed with tetrahydrofuran and acetone (30 mL × 3), and thoroughly cleaned by Soxhlet extraction with tetrahydrofuran for 10 h. Finally, it is vacuum-dried at 120 ℃ under reduced pressure (-0.09 MPa) for 12 h, the final product COF-C_4N/THQ-Co in black solid form. COF-C_4N/THQ-Fe, COF-C_4N/THQ-Co_1Fe_2, and COF-C_4N/THQ-Co_2Fe_1 were synthesized using the same procedure.

Synthesis of COF-C_4N+THQ-M: The prepared COF-C_4N samples were mixed with THQ-M samples at a mass ratio of 1:1 and ultrasonically dispersed by adding ethanol for 30 min, followed by stirring for 24 h. At the end of the reaction, filtration-washing-drying were carried out to obtain a simple composite COF-C_4N+THQ-M composite catalyst.

4.3 Materials Characterizations

The structure, composition, and texture properties of the materials are studied by using powder X-ray (PXRD) diffraction (TD-3700 X-ray diffractometer), Fourier transform infrared (FT-IR) (Equiox 55), scanning electron microscopy (SEM) micrographs (EVO18), and transmission electron microscopy (TEM) experiment (JEM-2100 electron microscope). X-ray photoelectron spectroscopy (XPS) measurements are using Thermo Scientific K-Alpha and the C 1s peak at 284.6 eV as the internal standard. Inductively Coupled Plasma-Optical Emission Spectrometry (ICP-OES) was carried out by using an Agilent ICP-OES 725 ES. The Nitrogen adsorption/desorption isotherms were evaluated at 77.3 K on Autosorb-1Q3, and the methods of Brunauer-Emmett-Teller (BET) and Barrett-Joyner-Halenda (BJH) were applied to get specific surface area and pore size distribution.

4.4 Electrochemical measurements

All the electrochemical measurements were conducted at room temperature using a standard three-electrode CHI660E (Shanghai Chenhua) electrochemical workstation. The Ag/AgCl and a graphite rod were used as reference and counter electrodes, respectively, and conductive carbon cloth fibers with deposited catalysts were used as working electrodes for evaluating the HER and OER activity of various catalysts. Electrochemical experiments were carried out on HER and OER in 1.0 M KOH solution. Before the electrochemical measurements, the 1.0 M KOH alkaline electrolyte was purged with N_2 gas for 30 min. All potentials at the reversible hydrogen electrode (RHE) were reported and converted using the equation (Eq. (1)).

$$\mathbf{E_{VS.\,RHE} = E_{VS.\,Ag/AgCl} + 0.2046\ V + 0.059\ V \times pH} \quad (1)$$

For the cyclic voltammetry (CV) tests, the potential range was circularly scanned at the OER potential range of 0~1.0 V (vs. Ag/AgCl) and the HER potential range of -1~ -1.82 V (vs. Ag/AgCl) at a scan rate of 50 mV s^{-1}. After 20 cycles of CV, the linear sweep voltammetry (LSV) test was conducted at a scan rate of 5 mV s^{-1} over the same potential range. The HER and OER overpotentials (η) were calculated according to the following Eq. (2) and (3).

$$\mathbf{\eta_{OER} = E_{VS.\,RHE} - 1.23\ V} \quad (2)$$

$$\mathbf{\eta_{HER} = E_{VS.\,RHE}} \quad (3)$$

The Tafel slope was estimated by linear fitting of the polarization curves according to the Tafel Eq. (4).

$$\mathbf{\eta = a + b\ log(j)} \quad (4)$$

Where j is the current density and b is the Tafel slope.

To evaluate the double-layer capacitance (C_{dl}), the CV was tested by applying different scan rates over a specific voltage range, and the difference in current density at the midpoint of the voltage range was selected for processing, which was linearly related to the corresponding scan rate, where the slope is the C_{dl} value. The active surface area of the catalyst can be inferred by comparing the C_{dl} size of several samples.

The electrochemical impedance spectroscopy (EIS), with potential conditions corresponding to a current density of 10 mA cm^{-2}, is performed in the frequency range of 0.01 Hz to 105 Hz, and data such as internal resistance and charge transfer resistance of different samples are compared by analyzing the test curves. The chronoamperometric measurement at constant potentials of 1.58 V (vs. RHE) and -0.18 V (vs. RHE) was performed to test the HER and OER stability of the samples.

Mott-Schottky tests were performed in a three-electrode cell using the Ag/AgCl electrode as the reference electrode. Using 500, 700, and 900 Hz to test the curve.

The TOF calculation. The turnover frequency (TOF) for each active site was determined employing methods previously reported. First, we performed cyclic voltammograms in phosphate buffer (pH = 7) with a scan rate of 50 mV s^{-1} to examine the number of active sites (n). Then, the number of voltammetric charges (Q) can be obtained after the blank value has been deducted. Therefore, n (mol) and TOF (s^{-1}) can be determined toward HER with the following Eq. (5) and Eq. (6).

$$\mathbf{n = \frac{Q}{2F}} \quad (5)$$

$$\mathbf{TOF = \frac{j \times S_{geo}}{2 \times n \times F}} \quad (6)$$

Toward OER, the n (mol) and TOF (s^{-1}) can be determined with the following equation:

$$\mathbf{n = \frac{Q}{4F}} \quad (7)$$

View Article Online
DOI: 10.1039/D5IM00302D

$$\mathbf{TOF} = \frac{\mathbf{j}\times\mathbf{S_{geo}}}{\mathbf{4}\times\mathbf{n}\times\mathbf{F}} \quad (8)$$

Where j is the measured current density, S_{geo} (1.0 cm^2) is the surface area of CFC, and F is the Faraday constant (96485.3 C mol^{-1}).

4.5 Calculation methods

Density Functional Theory (DFT) was used to calculate all geometrical and electron structures. The interaction between the core and valence electrons is described using the frozen-core projector augmented wave (PAW) approach.[51-53] The generalized gradient approximation of the Perdew-Burke-Ernzerhof (PBE) functional is used.[53] The energy cutoff is set to be 500 eV. A Γ-centered mesh of 3 × 3 × 1 k-points is used to sample the two-dimensional Brillöuin zone. The van der Waals (vdW) correction proposed by Grimme is adopted to describe long-range vdW interactions. A vacuum space greater than 15 Å perpendicular to the sheet is applied so that the interaction between neighboring slabs is negligible. All geometry structures are fully relaxed until the convergence criteria of energy and force are less than 1×10^{-5} eV and 0.01 eV $Å^{-1}$, respectively.

The binding energies of H, OH, and H_2O are calculated as Eq. (9) - (11).

$$\mathbf{\Delta E_H^b = E_{H*} - E_* - 0.5E_{H_2}} \quad (9)$$

$$\mathbf{\Delta E_{H_2O}^b = E_{H_2O*} - E_* - E_{H_2O}} \quad (10)$$

$$\mathbf{\Delta E_{OH}^b = E_{OH*} - E_* - E_{H_2O} + 0.5E_{H_2}} \quad (11)$$

where E_{H*}, E_{OH*}, and E_{H2O*} are the energies of H, OH, and H_2O absorbed on the catalyst surface. E_{H2O*} is the energy of the H_2O molecule in the gaseous phase.

Calculation of free energy difference: The free energy difference for OER is calculated according Eq. (12) to the computational hydrogen electrode model originally proposed by Nørskov and coworkers.[54, 55]

$$\mathbf{\Delta G = \Delta E + \Delta E_{ZPE} - T\Delta S + \Delta G_{pH} + \Delta G_U} \quad (12)$$

Where ΔE is the difference in electronic energy before and after adsorption, and ΔE_{ZPE}, T, and ΔS represent the zero-point energy correction, temperature, and entropy change of the adsorption system, respectively. For computing thermodynamic properties, the thermodynamic conditions are set to be 1 atmosphere and 298 K. The pH dependence of the reduction potential is given by ΔG_{pH} = 0.059 × pH, which stems from the H^+ concentration dependence of the entropy. ΔG_U is the contribution of the applied electrode potential (U) to ΔG.[56, 57]

OER involves four electron steps, which can be written as Step1-4 oxidation reaction equations:

$$*+OH^- \rightleftharpoons *OH+e^- \quad \text{(step 1)}$$

$$*OH+OH^- \rightleftharpoons *O+H_2O+e^- \quad \text{(step 2)}$$

$$*O+OH^- \rightleftharpoons *OOH+e^- \quad \text{(step 3)}$$

$$*OOH+OH^- \rightleftharpoons *+O_2+H_2O+e^- \quad \text{(step 4)}$$

Meanwhile, HER involves two-electron steps in alkaline conditions, which can be written as Step 5-7 reduction reaction equations:

$$* + H_2O + e^- \rightleftharpoons *H_2O \quad \text{(step 5)}$$

$$*H_2O \rightleftharpoons *H + OH^- \quad \text{(step 6)}$$

$$*H + H_2O + e^- \rightleftharpoons *+H_2+OH^- \quad \text{(step 7)}$$

where * denotes the adsorption site, *(radical) denotes the intermediate species adsorbed on the surface.

Considering the contribution from the zero-point energy, the entropy, the pH dependence of the redox potential, and the external potential supplied by the carrier, the free-energy changes along the reaction pathway for OER can be expressed as Eq. (13-16).[58]

$$\Delta G_{*OH} = G_{*OH} + 1/2G_{H_2} - G_* - G_{H_2O} - \Delta G_{pH} - eU \quad (13)$$

$$\Delta G_{*O} = G_{*O} + G_{H_2} - G_* - G_{H_2O} - 2\Delta G_{pH} - 2eU \quad (14)$$

$$\Delta G_{*OOH} = G_{*OOH} + 3/2G_{H_2} - G_* - 2G_{H_2O} - 3\Delta G_{pH} - 3eU \quad (15)$$

$$\Delta G_{*O_2} = 2G_{H_2} + G_{O_2} - 2G_{*H_2O} - 4\Delta G_{pH} - 4eU \quad (16)$$

The free-energy changes along the reaction pathway for HER can be expressed as Eq. (17-19).

$$\Delta G_{*H_2O} = G_{*H_2O} - G_{H_2O} - G_* + \Delta G_{pH} - eU \quad (17)$$

$$\Delta G_{*H} = G_{*H} - 1/2G_{H_2} - G_* + \Delta G_{pH} - eU \quad (18)$$

$$\Delta G_{*H_2} = 2\Delta G_{pH} - 2eU \quad (19)$$

Data availability

The data that support the findings of this study are available from the corresponding author upon reasonable request.

Author Contributions

Journal Name ARTICLE

Yang Liu: Writing - original draft, Methodology, Investigation. Zhao-Di Yang: Writing - review & editing, Supervision, Conceptualization. Rui Zhang: Investigation. Yingchao Lai: Investigation. Yu Zhang: Writing - Review & editing. Guiling Zhang: Supervision, Conceptualization.

View Article Online DOI: 10.1039/D5IM00302D

Conflicts of interest

The authors declare no conflict of interest.

Acknowledgements

This work was financially supported by the National Natural Science Foundation of China (Grant No. 52273288), National Key R&D Program of China (Grant No.2022YFC3901800), and Heilongjiang Provincial Natural Science Foundation of China (Grant No. LH2024B016).

References

1. Y. Liu, Y. Chen, Y. Tian, T. Sakthivel, H. Liu, S. Guo, H. Zeng and Z. Dai, Synergizing hydrogen spillover and deprotonation by the internal polarization field in a MoS_2/$NiPS_3$ vertical heterostructure for boosted water electrolysis, *Adv. Mater.*, 2022, **34**, 2203615.
2. G. B. Liu, Y. S. Xu, T. Yang and L. H. Jiang, Recent advances in electrocatalysts for seawater splitting, *Nano Mater. Sci.*, 2023, **5**, 101-116.
3. Y. Wang, J. Li, P. J. Yang, H. D. Li, G. R. Xu, Y. M. Du, C. X. Li, W. Jin, T. Y. Ma, Z. X. Wu and L. Wang, Interfacial Ru nanoclusters in tandem with single atoms on oxygen-vacancy regulated CeO_2 for anion exchange membrane seawater-splitting, *J. Energy Chem.*, 2025, **102**, 618-627.
4. W. J. Liu, M. Zhou, J. W. Zhang, W. X. Liu, D. D. Qin, Q. Liu, G. Z. Hu and X. J. Liu, Construction of a CoP/MnP/Cu_3P heterojunction for efficient methanol oxidation-assisted seawater splitting, *Mater. Chem. Front.*, 2025, **9**, 953-964.
5. R. Wu, J. Xu, C.-L. Zhao, X.-Z. Su, Z.-L. Zhang, Y.-R. Zheng, F.-Y. Yang, X.-S. Zheng, J.-F. Zhu, J. Luo, W.-X. Li, M.-R. Gao and S.-H. Yu, Dopant triggered atomic configuration activates water splitting to hydrogen, *Nat. Commun.*, 2023, **14**, 2306.
6. Y. W. Gui, Z. T. Liu, X. B. Feng, Y. F. Jia, Y. M. Zhang, Y. M. Zhang, H. Y. Yang, Y. Zhang, M. Y. Li, L. Liang and J. W. Shi, One-step electrodeposition synthesis of NiFePS on carbon cloth as self-supported electrodes for electrochemical overall water splitting, *J. Colloid Interface Sci.*, 2024, **673**, 444-452.
7. M. S. Yang, J. Y. Ding, Z. W. Wang, J. W. Zhang, Z. M. Peng and X. J. Liu, NiMo-based alloy and its sulfides for energy-saving hydrogen production via sulfion oxidation assisted alkaline seawater splitting, *Chin. Chem. Lett.*, 2025, **36**, 110861.
8. Z. S. Li, B. L. Li, M. Yu, C. L. Yu and P. K. Shen, Amorphous metallic ultrathin nanostructures: a latent ultra-high-density atomic-level catalyst for electrochemical energy conversion, *Int. J. Hydrogen Energy*, 2022, **47**, 26956-26977.
9. K. Song, H. Zhang, Z. Lin, Z. Wang, L. Zhang, X. Shi, S. Shen, S. Chen and W. Zhong, Interfacial engineering of cobalt thiophosphate with strain effect and modulated electron structure for boosting electrocatalytic hydrogen evolution reaction, *Adv. Funct. Mater.*, 2024, **34**, 2312672.
10. R. Yin, Z. Wang, J. Zhang, W. Liu, J. He, G. Hu and X. Liu, Tunable NiSe-Ni_3Se_2 heterojunction for energy-efficient hydrogen production by coupling urea degradation. *Small Methods*, 2025, **9**, 2401976.
11. D. Sui, R. S. Luo, S. M. Xie, H. Zhang, T. T. Ma, H. Sun, T.-T. Jia, J. Sun and X. Y. Li, Atomic ruthenium doping in collaboration with oxygen vacancy engineering boosts the hydrogen evolution reaction by optimizing H absorption, *Chem. Eng. J.*, 2024, **480**, 148007.
12. J. N. Hansen, H. Prats, K. K. Toudahl, N. M. Secher, K. Chan, J. Kibsgaard and I. Chorkendorff, Is there anything better than Pt for HER?, *ACS Energy Lett.*, 2021, **6**, 1175.
13. X. Chen, X.-T. Wang, J.-B. Le, S.-M. Li, X. Wang, Y.-J. Zhang, P. Radjenovic, Y. Zhao, Y.-H. Wang, X.-M. Lin, J.-C. Dong and J.-F. Li, Revealing the role of interfacial water and key intermediates at ruthenium surfaces in the alkaline hydrogen evolution reaction, *Nat. Commun.*, 2023, **14**, 5289.
14. Q. He, Y. Zhou, H. Shou, X. Wang, P. Zhang, W. Xu, S. Qiao, C. Wu, H. Liu, D. Liu, S. Chen, R. Long, Z. Qi, X. Wu and L. Song, Synergic reaction kinetics over adjacent ruthenium sites for superb hydrogen generation in alkaline media, *Adv. Mater.*, 2022, **34**, 2110604.
15. Y. Zheng, Y. Jiao, A. Vasileff and S.-Z. Qiao, The hydrogen evolution reaction in alkaline solution: From theory, single crystal models, to practical electrocatalysts, *Angew. Chem. Int. Ed.*, 2018, **57**, 7568.
16. H. Zhao, D. Chen, R. Yu, J. Jiao, W. Zeng, J. Zhu, X. Mu, Y. Yao, D. Wu, Y. Zhang, J. Wu and S. Mu, Atomizing platinum for hydrogen electrode reactions, *Nano Energy*, 2024, **121**, 109247.
17. X. A. Teng, Z. B. Wang, Y. S. Wu, Y. Zhang, B. Yuan, Y. Y. Xu, R. M. Wang and A. X. Shan, Enhanced alkaline hydrogen evolution reaction of MoO_2/Ni_3S_2 nanorod arrays by interface engineering, *Nano Energy*, 2024, **122**, 109299.
18. H. Ren, Z. Zhang, Z. Geng, Z. Wang, F. Shen, X. Liang, Z. Cai, Y. Wang, D. Cheng, Y. Cao, X. Yang, M. Hu, X. Yao and K. Zhou, Gradient OH desorption facilitating alkaline hydrogen evolution over ultrafine quinary nanoalloy, *Adv. Energy Mater.*, 2024, **14**, 2400777.
19. Y.-N. Zhou, W.-L. Yu, H.-J. Liu, R.-Y. Fan, G.-Q. Han, B. Dong and Y.-M. Chai, Self-integration exactly constructing oxygen-modified MoNi alloys for efficient hydrogen evolution, *EcoEnergy*, 2023, **1**, 425-436.
20. J. J. Yan, Y. Chang, J. X. Chen, M. L. Jia and J. C. Jia, Understanding the copper-iridium nanocrystals as highly effective bifunctional pH-universal electrocatalysts for water splitting, *J. Colloid Interface Sci.*, 2023, **642**, 779-788.
21. Y. Chen, Y. D. Liu, W. F. Zhai, H. Liu, T. Sakthivel, S. W. Guo and Z. F. Dai, Metastabilizing the ruthenium clusters by interfacial oxygen vacancies for boosted water splitting electrocatalysis, *Adv. Energy Mater.*, 2024, **14**, 2400059.
22. S. Anantharaj, S. Kundu and S. Noda, " The Fe effect ": A review unveiling the critical roles of Fe in enhancing OER activity of Ni and Co based catalysts, *Nano Energy*, 2021, **80**, 105514.
23. C. Li, H. Zhang, M. Liu, F.-F. Lang, J. D. Pang and X.-H. Bu, Recent progress in metal-organic frameworks (MOFs) for electrocatalysis, *Ind. Chem. Mater.*, 2023, **1**, 9-38.

View Article Online
DOI: 10.1039/D5IM00302D

24. Z. Di, C. Liu, J. Pang, C. Chen, F. Hu, D. Yuan, M. Wu and M. Hong, Cage-like porous materials with simultaneous high C_2H_2 storage and excellent C_2H_2/CO_2 separation performance, *Angew. Chem. Int. Ed.*, 2021, **60**, 10828-10832.
25. L. Kong, M. Liu, H. Huang, Y. Xu and X.-H. Bu, Metal/covalent-organic framework based cathodes for metal-ion batteries, *Adv. Energy Mater.*, 2022, **12**, 2100172.
26. B. Geng, F. Yan, X. Zhang, Y. He, C. Zhu, S.-L. Chou, X. Zhang and Y. Chen, Conductive CuCo-based bimetal organic framework for efficient hydrogen evolution, *Adv. Mater.*, 2021, **33**, e2106781.
27. Z. Qiu, Y. Li, Y. Gao, Z. Meng, Y. Sun, Y. Bai, N.-T. Suen, H.-C. Chen, Y. Pi and H. Pang, 2D MOF-assisted pyrolysis-displacement-alloying synthesis of high-entropy alloy nanoparticles library for efficient electrocatalytic hydrogen oxidation, *Angew. Chem. Int. Ed.*, 2023, **62**, e202306881.
28. Q. N. Liang, J. M. Chen, F. L. Wang and Y. W. Li, Transition metal-based metal-organic frameworks for oxygen evolution reaction, *Coord. Chem. Rev.*, 2020, **424**, 213488.
29. Y. K. Song, W. F. Xie, M. F. Shao and X. Duan, Integrated electrocatalysts derived from metal organic frameworks for gas-involved reactions, *Nano Mater. Sci.*, 2023, **5**, 161-176.
30. Y. S. Wei, M. Zhang, M. Kitta, Z. Liu, S. Horike and Q. Xu, A single-crystal open-capsule metal-organic framework, *J. Am. Chem. Soc.*, 2019, **141**, 7906-7916.
31. J. W. Li, P. Liu, J. X. Mao, J. X. Yan and W. B. Song, Two-dimensional conductive metal-organic frameworks with dual metal sites toward the electrochemical oxygen evolution reaction, *J. Mater. Chem. A*, 2021, **9**, 1623-1629.
32. Y. Lian, W. Yang, C. Zhang, H. Sun, Z. Deng, W. Xu, L. Song, Z. Ouyang, Z. Wang, J. Guo and Y. Peng, Unpaired 3d electrons on atomically dispersed cobalt centres in coordination polymers regulate both oxygen reduction reaction (ORR) activity and selectivity for use in zinc-air batteries, *Angew. Chem. Int. Ed.*, 2020, **59**, 286-294.
33. D. N. Xing, Y. Y. Wang, P. Zhou, Y. Y. Liu, Z. Y. Wang, P. Wang, Z. K. Zheng, H. F. Cheng, Y. Dai and B. B. Huang, Co_3(hexaiminotriphenylene)$_2$: A conductive two-dimensional π-d conjugated metal-organic framework for highly efficient oxygen evolution reaction, *Appl. Catal. B: Environ.*, 2020, **278**, 119295.
34. J. Park, A. C. Hinckley, Z. H. Huang, D. W. Feng, A. A. Yakovenko, M. Lee, S. C. Chen, X. D. Zou and Z. N. Bao, Synthetic routes for a 2D semiconductive copper hexahydroxybenzene metal-organic framework, *J. Am. Chem. Soc.*, 2018, **140**, 14533-14537.
35. Q. Jiang, P. Xiong, J. Liu, Z. Xie, Q. Wang, X.-Q. Yang, E. Hu, Y. Cao, J. Sun, Y. Xu and L. Chen, A redox-active 2D metal-organic framework for efficient lithium storage with extraordinary high capacity, *Angew. Chem. Int. Ed.*, 2020, **59**, 5273-5277.
36. Z. Guo, S. Yang, M. Liu, Q. Xu and G. Zeng, Construction of core-shelled covalent/metal-organic frameworks for oxygen evolution reaction, *Small*, 2024, **20**, 2308598.
37. M. H. Liu, Q. Xu, Q. Y. Miao, S. Yang, P. Wu, G. J. Liu, J. He, C. B. Yu and G. F. Zeng, Atomic Co-N_4 and Co nanoparticles confined in COF@ZIF-67 derived core-shell carbon frameworks: Bifunctional non-precious metal catalysts toward the ORR and HER, *J. Mater. Chem. A*, 2022, **10**, 228-233.
38. G. F. Li, D. Wang, Q. Xing, G. Zhou, S. Liu, Y. Li, L. Zheng, P. Ye and J. Zou, Design and syntheses of MOF/COF hybrid materials via postsynthetic covalent modification: An efficient strategy to boost the visible-light-driven photocatalytic performance, *Appl. Catal. B*, 2019, **243**, 621-628.
39. H. Peng, J. Raya, F. Richard, W. Baaziz, O. Ersen, A. Ciesielski and P. Samori, Synthesis of robust MOFs@COFs porous hybrid materials via an Aza-Diels-Alder reaction: Towards high-performance supercapacitor materials, *Angew. Chem. Int. Ed.*, 2020, **59**, 19602-19609.
40. S. Zhou, Y. Kuang, H. Yang, L. Gan, X. Feng, C. Mao, L. Chen, J. Zheng and G. Ouyang, Structure-controlled interpenetrated MOF@COF via C-C linkage for enhanced photocatalysis, *Angew. Chem. Int. Ed.*, 2024, **62**, e202412279.
41. J. H. Li, P. X. Liu, Y. Chen, J. F. Zhou, J. W. Li, J. F. Yang, D. L. Zhang, J. P. Li and L. B. Li, A customized hydrophobic porous shell for MOF-5, *J. Am. Chem. Soc.*, 2023, **145**, 19707-19714.
42. M. Gao, M. Qi, L. Liu and Z. Han, An exceptionally stable core-shell MOF/COF bifunctional catalyst for a highly efficient cascade deacetalization-Knoevenagel condensation reaction, *Chem. Commun.*, 2019, **55**, 6377-6380.
43. C. H. Yang, Z.-D. Yang, H. Dong, N. Sun, Y. Lu, F.-M. Zhang and G. L. Zhang, Theory-driven design and targeting synthesis of a highly-conjugated basal-plane 2D covalent organic framework for metal-free electrocatalytic OER, *ACS Energy Lett.*, 2019, **4**, 2251-2258.
44. L. Zhao, J. Yan, H. Huang, X. Du, H. Chen, X. He, W. Li, W. Fang, D. Wang, X. Zeng, J. Dong and Y. Liu, Regulating electronic structure of bimetallic NiFe-THQ conductive metal-organic frameworks to boost catalytic activity for oxygen evolution reaction, *Adv. Funct. Mater.*, 2024, **34**, 2310902.
45. J. Zhao, Y. Zhang, H. Lu, Y. Wang, X. D. Liu, M. K. S. Hirbod, J. Peng, S. Chen, X. Li and Y. Zhang, Additive manufacturing of two-dimensional conductive metal-organic framework with multidimensional hybrid architectures for high-performance energy storage, *Nano Lett.*, 2022, **22**, 1198-1206.
46. G. Chen, L. B. Gee, W. Xu, Y. Zhu, J. S. Lezama-Pacheco, Z. Huang, Z. Li, J. T. Babicz, S. Choudhury, T.-H. Chang, E. Reed, E. I. Solomon and Z. Bao, Valence-dependent electrical conductivity in a 3D tetrahydroxyquinone-based metal-organic framework, *J. Am. Chem. Soc.*, 2020, **142**, 21243-21248.
47. J. M. Wei, M. Zhou, A. C. Long, Y. M. Xue, H. B. Liao, C. Wei and Z. C. J. Xu, Heterostructured electrocatalysts for hydrogen evolution reaction under alkaline conditions, *Nano-Micro Lett.*, 2018, **10**, 75.
48. J. Zhu, L. S. Hu, P. X. Zhao, L. Y. S. Lee and K.-Y. Wong, Recent advances in electrocatalytic hydrogen evolution using nanoparticles, *Chem Rev.*, 2020, **120**, 851-918.
49. M. Cabán-Acevedo, M. L. Stone, J. R. Schmidt, J. G. Thomas, Q. Ding, H.-C. Chang, M.-L. Tsai, J.-H. He, and S. Jin, Efficient hydrogen evolution catalysis using ternary pyrite-type cobalt phosphosulphide, *Nat. Mater.*, 2015, **14**, 1245-1251.
50. J. Q. Tian, Q. Liu, A. M. Asiri, and X. P. Sun, Self-supported nanoporous cobalt phosphide nanowire arrays: An efficient 3D hydrogen-evolving cathode over the wide range of pH 0-14, *J. Am. Chem. Soc.*, 2014, **136**, 7587-7590.
51. G. Kresse and J. Hafner, Ab initio molecular dynamics for liquid metals, *J. Phys. Rev. B*, 1993, **47**, 558.
52. G. Kresse and J. Hafner, Ab initio molecular-dynamics simulation of the liquid-metal- amorphous-semiconductor transition in germanium, *Phys. Rev. B*, 1994, **49**, 14251.
53. P. E. Blöchl, Projector augmented-wave method, *Phys. Rev. B*, 1994, **50**, 17953.

54. J. G. Howalt, T. Bligaard, J. Rossmeisl and T. Vegge, DFT based study of transition metal nano-clusters for electrochemical NH_3 production, *Phys. Chem. Chem. Phys.*, 2013, **15**, 7785-7795.
55. J. K. Nørskov, J. Rossmeisl, A. Logadottir, L. Lindqvist, J. R. Kitchin, T. Bligaard and H. Jónsson, Origin of the overpotential for oxygen reduction at a fuel-cell cathode, *J Phys. Chem. B*, 2004, **108**, 17886-17892.
56. A. A. Peterson, F. A. Pedersen, F. Studt, J. Rossmeisl and J. K. Nørskov, How copper catalyzes the electroreduction of carbon dioxide into hydrocarbon fuels, *Energy Environ. Sci.*, 2010, **3**, 1311-1315.
57. G. Ertl, S. B. Lee and M. Weiss, Kinetics of nitrogen adsorption on Fe(111), *Surf. Sci.*, 1982, **114**, 515-526.
58. Y. Y. Wan, L. Wang, H. X. Xu, X. J. Wu and J. L. Yang, A simple molecular design strategy for two-dimensional covalent organic framework capable of visible-light-driven water splitting, *J. Am. Chem. Soc.*, 2020, **142**, 4508-4516.

View Article Online
DOI: 10.1039/D5IM00302D

View Article Online
DOI: 10.1039/D5IM00302D

Data availability Statement

The data that support the findings of this study are available from the corresponding author upon reasonable request.